A homogenization study of the effects of cycling on the electronic conductivity of commercial lithium-ion battery cathodes

J. M. Foster, A. Gully, H. Liu, S. Krachkovskiy, Y. Wu, S. B. Schougaard, M. Jiang, G. Goward, G. A. Botton & B. Protas

August 31, 2016

Abstract

State-of-the-art image acquisition, image analysis and modern homogenization theory are used to study the effects of cycling on commercial lithium-ion battery cathodes' ability to conduct electronic current. This framework allows for a rigorous computation of an effective, or macroscale, electronic conductivity given an arbitrarily complicated three-dimensional microstructure comprised of three different material phases – *i.e.*, active material, binder (polymer mixed with conductive carbon black), and electrolyte. The approach explicitly takes into account the geometry, and is thus a vast improvement over the commonly used Bruggeman approximation. We apply our framework to two different types of lithium-ion battery cathodes before and after cycling. This leads us to predict an appreciable decrease in the effective electronic conductivity as a direct result of cycling. In addition, we present an ad-hoc 'neighbour counting' methodology which meaningfully quantifies the effect of binder detaching from the surface of the active material due to the internal mechanical stresses experienced under operating conditions, thereby supporting the results of the homogenization calculations.

1 Introduction

A significant research effort is currently focused on the development of lithium-ion batteries for use in a variety of areas, *e.g.*, the automotive industry and consumer electronics, because they exhibit several desirable qualities including no memory effects, little self-discharge, and a comparably high energy density. Many previous studies have considered how to model the electrochemical processes occurring within such cells, with the aim of informing the optimal design. The majority of these studies have been (at least partially) based on the seminal works of Newman *et al.* [6; 7; 8; 9]. Providing an exhaustive list, or even summary, of the extant work on lithium-ion batteries would be almost impossible. Instead, we point the interested reader toward one of the many books now available on the physical chemistry of electrochemical systems including lithium-ion batteries [24]. Of particular interest is modeling that allows for optimization of energy density, charge/discharge rates, safety and cycling life. This contribution will focus on the latter, specifically the loss of efficacy of the electron transport in the electrode as it ages.

Lithium-ion batteries are comprised of four key constituents: (i) the anode (the negative electrode during discharge); (ii) the cathode (the positive electrode during discharge); (iii) the electrolyte, and; (iv) a porous separator that ensures unhindered passage of electrolyte (ionic current)

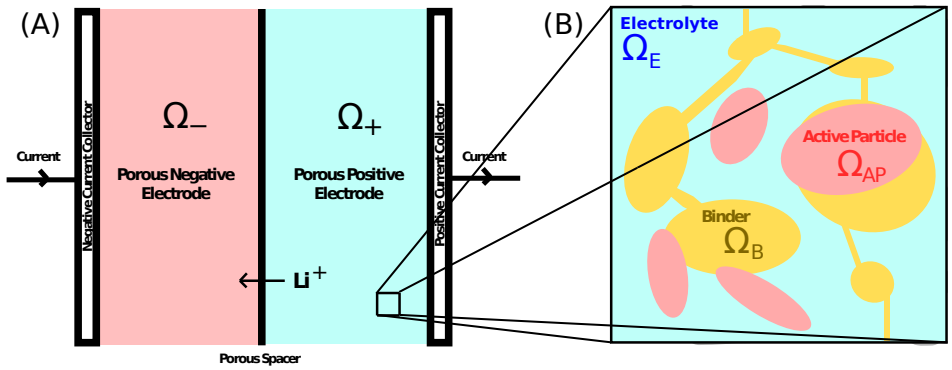

Figure 1: (A): A schematic of a cross section of a lithium-ion cell at the whole cell scale. (B): A schematic of the microstructure within the positive electrode. Here, three distinct material components are observed, namely, the active particle Ω_{AP}, the polymer binder Ω_B, and the electrolyte Ω_E.

while electronically isolating the two electrodes (figure 1). This assembly is sandwiched between two metallic current collectors, that connect to the external circuit, where energy is injected or removed from the system.

During operation, which can only be maintained when both the ionic and the electronic charges are transported between the two electrodes ensuring overall charge neutrality, the chemical potential difference between the positive and the negative electrodes leads to charge transfer events (redox reactions) in the active materials. In commercial cells both the anode and cathode have a complex morphology and are typically comprised of small particles of active material and binder – a polymer to which highly conductive carbon black has been added – which are compressed together to form a porous matrix into which the electrolyte can penetrate. This structure is employed in order to minimize the ionic and electronic charge transport paths within the active particles which is orders of magnitude more resistive than the binder and electrolyte. Importantly, cycling the active materials is accompanied by volumetric changes, which can be accommodated by the liquid electrolyte but may lead to permanent structural changes in the binder. In unfavourable cases, these structural changes are envisioned to have a detrimental effect on electronic charge transport pathways as the battery is cycled. Our aim here is to use high resolution 3D images of electrodes before and after cycling to determine the changes in the electrodes ability to conduct electronic current. To this end we apply two different analysis methods. First, we apply a 'neighbour-counting' technique which quantifies the connectedness, *i.e.* the extent of the delamination, between the surfaces of the active material particles and the binder. Second, we employ systematic modern homogenization (developed in [15]), in three spatial dimensions, to quantify the loss of electrical pathways within the binder (as measured by a decrease in the macroscale effective electronic conductivity). The effective electronic conductivity discussed here is defined such that the homogenized material carries exactly the same current density as the original three-phase composite material under the same imposed potential gradients. In other words, the effective electronic conductivity represents replacing a highly complex heterogeneous composite material with a simple homogeneous material which has precisely the same macroscale properties. The homogenization methodology employed in this study was originally developed and validated for use in the context of porous electrochemical electrode materials in [15]. In the present study, we utilize the tools presented in [15] to address some practical questions related to real cell degradation. In addition, we also generalize the existing framework so that it can be used in a 'nested' manner.

2 Experimental Methods

2.1 Cathode preparation

In this study, we employed commercial and laboratory-prepared electrodes, hereafter labelled NMC and HE-NMC respectively, based on a Li, Ni, Mn, Co layered oxides. These required slightly different preparation procedures as detailed below.

NMC cathodes: The manufacturers' original pouch casing contained around 30 interlaid cathode and anode pairs. The NMC cathodes were removed from the stack in their fully 'swollen'/lithiated state and cleaned using Dimethylcarbonate (DMC) to remove any traces of the commercial electrolyte. This was done under the protection of an argon atmosphere (O_2 ¡1.2 ppm and H_2O ¡0.1ppm) before inclusion in the 'half cell' (see below). We were unable to obtain precise details on the composition of the active NMC from the manufacturer. Thus, we limit the description of the active material to a nickel manganese cobalt oxide which has the form $LiNi_xMn_yCo_{1-x-y}O_2$. The binder in use was polyvinylidene fluoride (PVDF) to which carbon had been added.

HE-NMC cathodes: The HE-NMC cathodes were manufactured in-house. The active material powder, $Li[Li_{0.2}Mn_{0.54}Ni_{0.13}Co_{0.13}]O_2$, was synthesized using the co-precipitation method from stoichiometric amounts of the transition metal acetates: (i) $Ni(CH_3CO_2)_2{\cdot}xH_2O$ (99+%, Alfa Aesar); (ii) $Mn(CH_3CO_2)_2{\cdot}xH_2O$ (99+%, Acros Organics), and; (iii) $Co(CH_3CO_2)_2{\cdot}xH_2O$ (98+%, Alfa Aesar). These constituents were dissolved in de-ionized water and then added drop-by-drop to a solution of KOH (0.1 M) to form the mixed transition metal hydroxides. The precipitate was filtered and washed with de-ionized water to remove any residual KOH. After drying overnight at 100 °C in an air-oven, the co-precipitated hydroxides were mixed with a 3% excess of lithium hydroxide by grinding for half an hour, before being heated for 24 hours in air at 900 °C and then cooled in air. Cathodes were prepared under the protection of an argon atmosphere (O_2 ¡0.1 ppm and H_2O ¡0.1ppm) using a doctor-blade from a mixture of 80 wt-% active material with 10 wt-% Super P Carbon and 10 wt-% PTFE polymer in N-Methyl-2-pyrrolidone (NMP).

The cathodes were assembled into a 'half-cell' configuration by: (i) covering the cathode with a sheet of porous separator; (ii) adding a disc of lithium metal on the opposite side of the separator; (iii) bathing the whole assembly in an 1 M $LiPF_6$ ethylene carbonate/dimethyl carbonate electrolyte (1:2-v/v EC/DMC), and; (iv) encapsulating the assembly in a 'coin cell' casing.

2.2 Electrochemical testing

Cycling of NMC half cells was performed using a BioLogic VMP multipotentiostat at a rate of C/30 (1C=280mA/g) for 10 cycles followed by 10 cycles at C/10 between 4.5V and 3.3V. The HE-NMC cathodes were cycled using a Maccor cycler for a total of 50 cycles at a rate of C/3, using a protocol where the cells were charged to 4.6V and then held at a constant voltage until the current dropped to less than C/20, before discharge to a potential of 2.0V. To ensure a fair comparison of the pristine and cycled cathodes, all cells were fully discharged (cathodic active material fully lithiated/dilated) before imaging.

2.3 Image acquisition

A Zeiss NVision 40 dual-beam FIB/SEM instrument was used for serial sectioning. A thin layer of Tungsten was initially deposited on the sample surface to circumvent preferential thinning of

soft phases and to reduce the curtaining effect. A high-energy focused Ga-ion beam (with a 30keV incident energy) with a small spot size was generated and the localized material was removed by the interaction of these high-energy ions with the target sample. For each of the four cathodes around 280 serial images were obtained with approximately a 70nm spacing between each slice. The resolution of the usable sections of the 2D image plane was around 700×700 pixels, each of which had a size of around 35×35nm. Thus, the volume of each of the samples was around $24\mu m \times 24\mu m \times 20\mu m$. It is noteworthy that the pixel resolution in the 2D image plane is comparable to the slice spacing. This is especially important for our study, as it allows us to construct isotropic computational grids (with the same node spacing in different directions). Although the number of serial images, the spacing between slices and the total volume that was imaged was *slightly* different for each of the cathodes, care was taken that any small variations in the imaging process were properly accounted for when the images were processed. We ensured that in all cases, each voxel in the final segmented images corresponded to the same physical dimensions.

3 Theory

3.1 Image processing

The sequential set of FIB images must be digitally segmented into the three components of an electrode for further mathematical treatment, see figure 1B. Segmentation was performed using an in-house MATLAB code which identifies material phases based on their grey-scale values and gradients in those grey-scale values – for details see [15]. Each of the steps in the nested homogenization procedure requires different sections of the segmented FIB images. Details on the selection of appropriate image sections are given in the 'results' section below. Where needed, image compression was carried out using a nearest-neighbour 3D stencil with the selection based on the phase that occurs most frequently to yield a final segmented image of approximately 50×50×50 voxels. By splitting the homogenization process into multiple steps we ensure that the amount of compression needed to form a computational grid of a tractable size is always small – and, in many cases, no compression is necessary.

3.2 Neighbour counting analysis

The quantification of the connectivity/delamination between the binder phase and active material was obtained by 'scanning' along the rows of voxels in each of the three directions (x_1, x_2 and x_3), and counting the number of times a voxel of active particle is immediately adjacent to a voxel of binder. An in-house MATLAB code was written to automate this task.

3.3 Nested homogenization

Homogenization over two distinct length scales Modern homogenization techniques [4; 22; 27] are powerful tools that: (i) can be used to calculate effective transport properties of composite electrodes in three spatial dimensions with two distinct length scales (figure 2), and; (ii) when combined with the method of multiple scales, can be used to systematically derived effective macroscopic models ('upscaled' models) from microscopic descriptions, see *e.g.*, [16; 25; 26]. Here, we will be concerned with the former, in particular we will focus on computing the effective electronic conductivity of our cathode samples – it is noteworthy that while the focus here will be on electronic conductivity, the approach discussed in the remainder of this section could equally be applied to

compute a variety of other transport coefficients, *e.g.*, thermal conductivity or ionic diffusivity [15]. For the purpose of computing effective transport properties, in contrast to volume averaging, the method used here allows one to determine exactly (up to computational error) both the values of, and establish bounds on, the effective transport parameters. Although more complicated than volume averaging, as we shall demonstrate, our approach is still computationally tractable. Here, we use the analytic continuation method proposed by Bergman, Milton, Golden and Papanicolaou [3; 12; 19; 20] which separates geometrical information from material properties in a mathematically precise manner. Further, this formulation yields rigorous bounds on largest and smallest values of the effective electronic conductivity achievable with prescribed volume fractions. In the Supporting Information we present an extension of these rigorous bounds to a material with three (or more) distinct length scales and show that for a given geometry a sharper bound can be found. Here, we use this sharper upper bound to provide perspective on how well our cathode samples perform relative to optimal geometric configurations, see tables 3 and 4.

The effective electronic conductivity $\boldsymbol{\sigma}^*$ (hereafter, an asterisk will denote an effective property) will be determined based on the current induced in the composite material by a unit potential drop. Interfacial electrochemical effects, such as those described by the Butler-Volmer kinetics, are not taken into account since we are only concerned with the *transport* of electrons. We consider only *electronic* current, *i.e.*, current induced by the transport of electrons, and do not include the ionic current induced by the transport of charged ions. Formally, we require the following assumptions concerning the domain Ω_0 – which could, in general, be a section of either the negative or positive electrode (Ω_- or Ω_+, see figure 2).

Assumption 1

(a). Ω_0 *is periodic in all three directions,*

(b). Ω_0 *is a union of three subdomains* Ω_B, Ω_{AP} *and* Ω_E *which represent the binder, active particle and electrolyte phases respectively (see figure 2),* i.e., $\Omega_0 = \Omega_B \cup \Omega_{AP} \cup \Omega_E$,

(c). each of the phases Ω_j *(*j *=B, AP and E) is isotropic,*

(d). the individual phases are characterized by non-zero conductivity coefficients σ_j *(*j *=B, AP and E) such that*

$$\sigma(\boldsymbol{x}) = \sigma_B \chi_B(\boldsymbol{x}) + \sigma_{AP}\chi_{AP}(\boldsymbol{x}) + \sigma_E \chi_E(\boldsymbol{x}), \tag{1}$$

where

$$\chi_j(\boldsymbol{x}) := \begin{cases} 1 & \textit{for} \quad \boldsymbol{x} \in \Omega_j, \\ 0 & \textit{for} \quad \boldsymbol{x} \notin \Omega_j \end{cases} \tag{2}$$

is the characteristic function of the j*-th phase (":=" means equal to by definition).*

The homogenization methodology requires that the electrode microstructure is periodic in all three directions (assumption 1(a)). In principle, proper periodicity can always be assumed, however, this leads to sharp edges between material phases on the boundaries of the domain. Here, we elect to 'move' these sharp edges to the interior of the domain by 'stacking' the segmented electrode images side-by-side (figure 6). Ensuring periodicity in this manner leads to better computational efficiency and has previously been shown *not* to be a significant source of error [15].

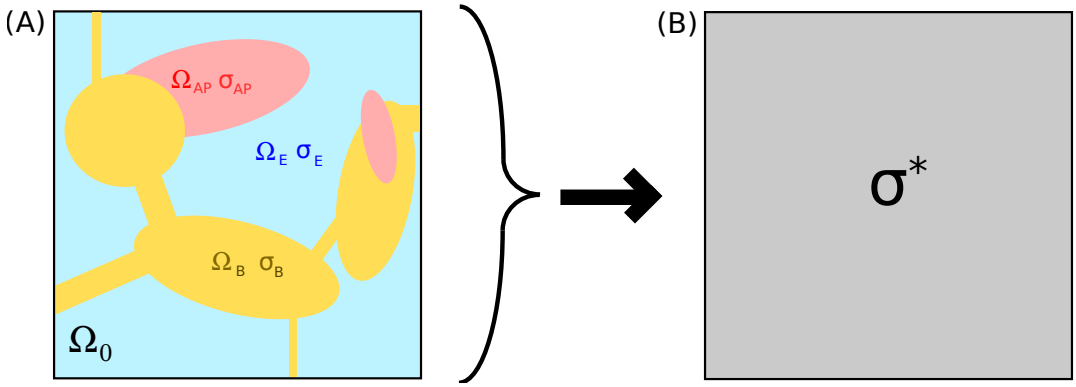

Figure 2: (A) A schematic of a cross section of an irregular periodic microstructure Ω_0 featuring three phases with distinct transport coefficients represented by the subdomains Ω_{AP} (red), Ω_E (blue) and Ω_B (yellow). (B) The corresponding homogenized material. From a macroscale point of view, both (A) and (B) have identical transport properties. The homogenized domain (B) is characterized by an effective electronic conductivity denoted with a star.

On denoting the current and electric fields by $\mathbf{J}$ and $\mathbf{E}$ respectively, Ohm's law becomes

$$\mathbf{J}(\mathbf{x}) = \sigma(\mathbf{x})\mathbf{E}(\mathbf{x}), \tag{3}$$

where $\sigma(\mathbf{x})$ is defined in equation (1). Since the electric field is the negative gradient of the electrical potential and there are no sources (or sinks) of charge within the material, we can write

$$\boldsymbol{\nabla} \times \mathbf{E}(\mathbf{x}) = 0 \quad \text{and} \quad \boldsymbol{\nabla} \cdot \mathbf{J}(\mathbf{x}) = 0. \tag{4}$$

On setting the electric field, $\mathbf{E}$, to unity oriented in the k-th direction, *i.e.* on setting

$$\langle \mathbf{E} \rangle = \mathbf{e}_k, \tag{5}$$

where $\mathbf{e}_k$ is a unit vector in the k-th direction for $k = 1, 2, 3$, the effective conductivity, $\boldsymbol{\sigma}^*$, which is a diagonal tensor, is defined via

$$\langle \mathbf{J} \rangle = \boldsymbol{\sigma}^* \langle \mathbf{E} \rangle. \tag{6}$$

Here, $\langle \cdot \rangle$ denotes the spatial average over a general periodic microstructure Ω_0. After some transformations, described in [15], a computational algorithm is obtained which allows us to conveniently evaluate the effective conductivity $\boldsymbol{\sigma}^*$. The process is broken into several steps that can be easily implemented using tools of finite-element analysis, such as those available in COMSOL [5]. Information about the microstructure (extracted from the segmented images) is imported as functions χ_B, χ_{AP} and χ_E using interpolation routines. For convenience, we also let $s_B := 1/(1 - \sigma_B/\sigma_E)$ and $s_{AP} := 1/(1 - \sigma_{AP}/\sigma_E)$. On introducing the operator $\boldsymbol{\Gamma}$ (following [11; 12; 13; 14]), defined for an arbitrary vector field $\mathbf{z}$ as $\boldsymbol{\Gamma}\mathbf{z} := \boldsymbol{\nabla}(-\Delta)^{-1}\boldsymbol{\nabla} \cdot \mathbf{z}$, we can express the resolvent of the electric field $\mathbf{E}$ as

$$\mathbf{E} = [\mathbf{I} + s_B^{-1}\boldsymbol{\Gamma}\chi_B + s_{AP}^{-1}\boldsymbol{\Gamma}\chi_{AP}]^{-1}\mathbf{e}_k \tag{7}$$

in which $\mathbf{I}$ is the identity operator. It can then be shown that

$$[\boldsymbol{\sigma}^*]_{kk} = \sigma_E \left[1 - \left\langle \mathbf{e}_k^T \left(s_B^{-1}\chi_B + s_{AP}^{-1}\chi_{AP}\right) [\mathbf{I} + s_B^{-1}\boldsymbol{\Gamma}\chi_B + s_{AP}^{-1}\boldsymbol{\Gamma}\chi_{AP}]^{-1}\mathbf{e}_k \right\rangle\right]. \tag{8}$$

It is by numerically solving equation (8), subject to periodic boundary conditions (in agreement with assumption 1(a)), that the effective conductivity tensor is found for any three-dimensional geometric configuration with three material phases, each with its own individual value of electronic conductivity. The solution is found without having to specifically track the electric and current fields within the composite material; however, these fields can be studied *a posteriori* via suitable post-processing, see for example panel (D) in figure 6. Finally, while the effective electronic conductivity can be computed in a variety of ways, the proposed approach has the advantage (over, *e.g.*, the Bruggeman approximation) of separating the geometric information about the microstructure from the material properties.

Extension to homogenization over three distinct length scales The extension of the homogenization approach to a material with three (or more) distinct length scales follows directly from the sequential application of the homogenization techniques described in section above. Here, we term this multi-step technique 'nested' homogenization. It should be noted that similar ideas have been used previously, see *e.g.* [2; 17; 18]. In those studies the multi-step homogenization technique was termed 're-iterated' homogenization. Although both approaches concern treatment of systems exhibiting more than two distinct length scales, the goal of 're-iterated' homogenization is to derive effective (upscaled) equations/operators, whereas 'nested' homogenization is used to calculate effective transport properties. 'Nested' homogenization refers to homogenization that is carried out recursively, one length scale at a time, and, at each stage carrying the results of previous homogenization steps forward (up the scales) in the form of calculated combined phases transport properties.

For Li-ion cell cathodes the 'nested' homogenization process is depicted in figure 3 - panel (A) shows a schematic, whilst panel (B) shows corresponding representative sections of the raw FIB images. As is evident from these images, there are three distinct length scales: the smallest, intermediate and largest scales are shown in panels (a)(i) and (a)(ii), (b) and (c), respectively. In the first step the electrolyte (blue) and active material phase (red) in (a)(i) are homogenized to yield the purple phase in figure 3 (b), and, the electrolyte (blue) and binder (yellow) phases in (a)(ii) are homogenized to give the green phase in (b). In the second step the three phases (blue, purple and green) shown in (b) are homogenized and become the grey phase in figure 3 (c). Provided that during each of the stages of homogenization the microstructure has the properties described in assumption 1, and that there is sufficient separation in length scales, this procedure is valid. This nested homogenization is of paramount importance here, as without these steps the resolution requirements would render solution of the problem (8) computationally intractable. Nested homogenization is thus an approximate procedure – with errors that can be made arbitrarily small – that allows one to split a multiscale problem with several different distinct length scales into subproblems, each of which corresponds to homogenization over a single length scale.

For both types of cathodes (NMC and HE-NMC) considered here, the two-level homogenization (or nested homogenization) is performed with one noteworthy exception, namely, that for the NMC cathodes there is no need to perform the first level of homogenization to compute a combined active particle and electrolyte phase, see figure 3 (a)(i), owing to the absence of the very small-scale electrolyte pores in the active particle, see panels (A) and (C) in figure 5 .

3.4 Computations

As discussed, computationally evaluating the effective electronic conductivity $\boldsymbol{\sigma}^*$ essentially involves solving equation (8), subject to periodic boundary conditions. This type of problem is readily solved using standard finite-element techniques [15]. The finite-element discretization was carried out using

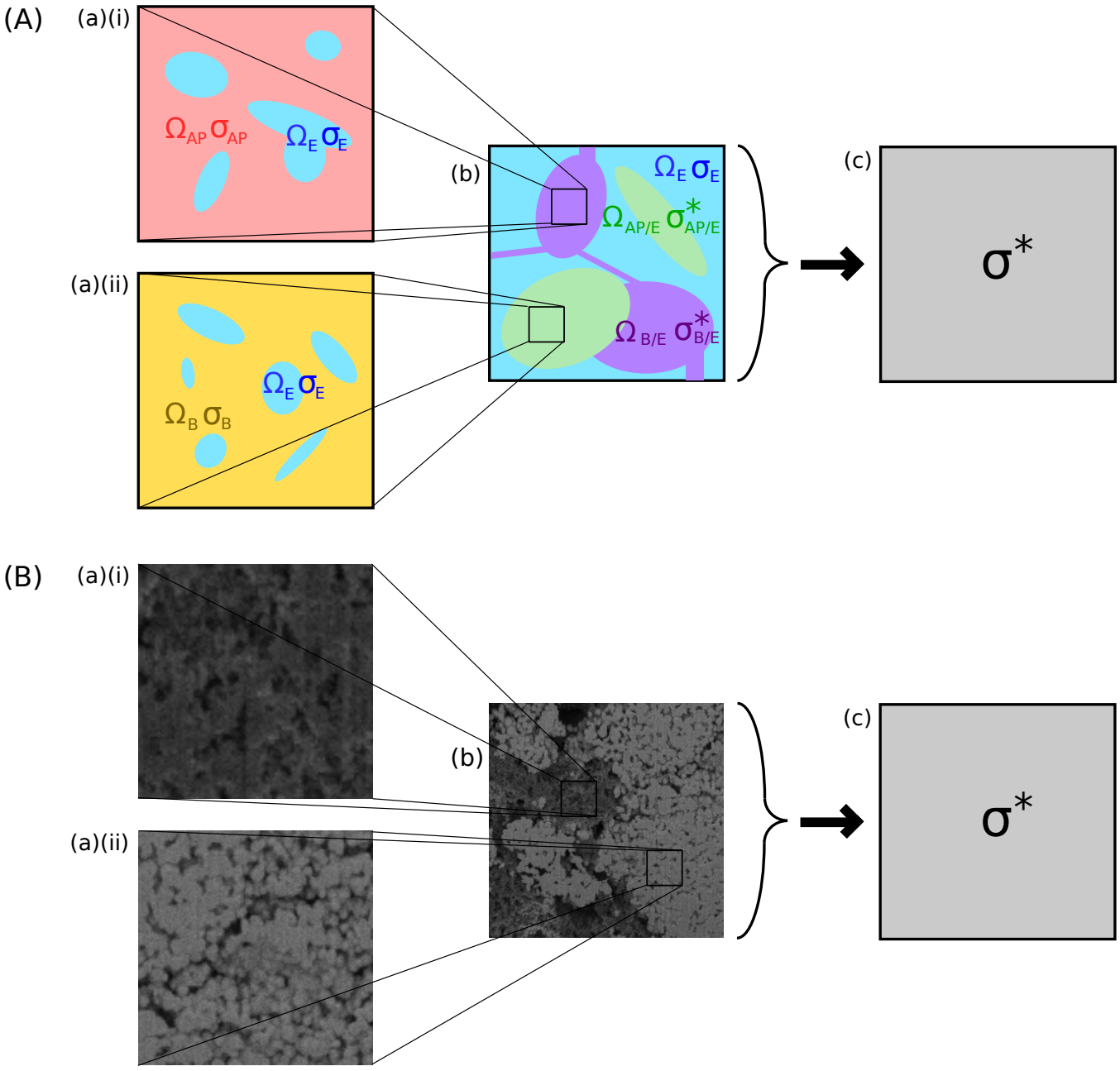

Figure 3: (A) A schematic of the 'nested' homogenization process, and; (B) some corresponding example FIB images of the HE-NMC cathode.

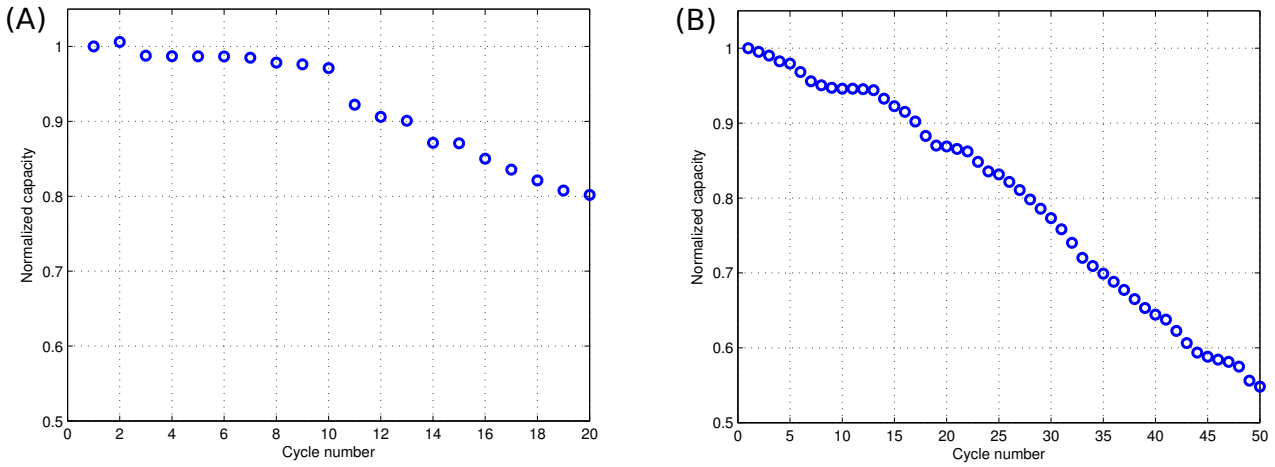

Figure 4: Normalized capacity against cycle number for, (A), the NMC cathode, and (B) the HE-NMC cathode. The capacity on the vertical axis has been normalized by the initial capacity.

the COMSOL Graphical User Interface which adaptively selects the order of the interpolation based on the stiffness of the system. We chose to solve the resulting algebraic system using the MUMPS algorithm because it is well suited to exploit the available shared-memory multicore architecture of the computer system — a 32-core 2.4 GHz AMD Opteron system with 128GB of RAM memory. In practice only around 35GB of RAM was needed. In order to obtain a sufficient number of significant digits of accuracy around 25 iterations were typically needed, and this took around 2 hours of computation time on our system.

4 Results

The electrochemical cycling was carried out under abusive conditions – the NMC and HE-NMC cathodes show significant capacity decay. After 20 and 50 cycles the remaining capacities are only approximately 80% and 55% of the initial value, respectively (figure 4).

Representative high-resolution microstructure images obtained with the FIB/SEM technique are shown in figure 5. Visual inspection of the images in figure 5 reveals some distinct differences between the two types of cathodes. In panels (A) and (C) the standard NMC cathode which has regions of pore-free active material (light grey) surrounded by a porous matrix of binder and carbon black (medium grey) that is interpenetrated with electrolyte (dark grey). Comparison of the pristine NMC cathode (A) with the same type of cathode after 20 cycles (C) indicate that the binder matrix appears to have slightly pulled away from the surfaces of the active particles during the cycling process. Inspecting the HE-NMC cathodes after one cycle (B) and after 50 cycles (D) we observe that the regions of active material are more particulate in nature – with many small scale electrolyte pores. Judging whether the binder matrix has also detached in these cathodes is more difficult, and more rigorous analysis – provided below – will be needed to quantify the changes in morphology that have occurred through cycling.

The results of the neighbour-counting analysis (table 1 and figure 7) shows that, for both pairs of cathodes, there is a marked decrease in the number of instances of active particle abutting the binder phase after cycling. This indicates that any decrease in effective electronic conductivity may, at least partially, be due to the delamination of the binder from the surfaces of the particles of active material. Although a quantitative comparison between this neighbour-counting analysis and

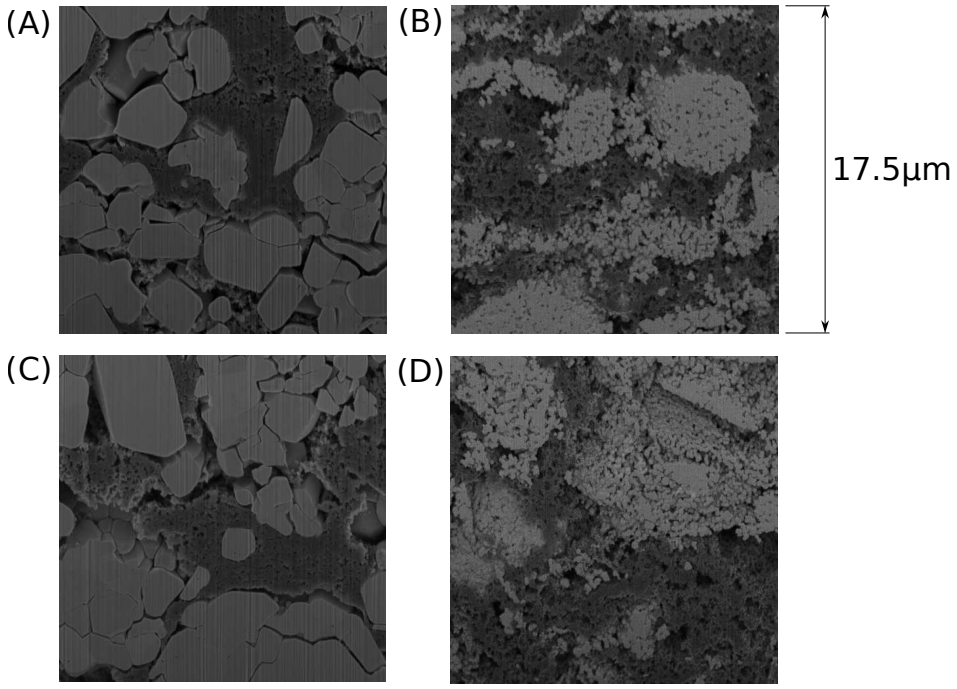

Figure 5: FIB/SEM images (in the $x_1 - x_2$ plane) from: (A) a pristine NMC cathode; (B) a HE-NMC cathode after one cycle; (C) a NMC cathode after twenty cycles, and; (D) a HE-NMC cathode after fifty cycles.

the results of the homogenization (presented below) is difficult, it is clear that the two approaches both concur that the geometrical changes that occur via cycling are detrimental to the conduction of electronic current through the electrode.

In order to carry out the nested homogenization procedure suitable values for the conductivities of the three constituent phases must be selected. In the literature there is a large discrepancy in the reported values of the electronic conductivity of NMC, PVDF/PTFE-based binders and EC/DMC-based electrolytes. The conductivities used in this work were therefore chosen within the range of literature values to ensure consistency with previous work (table 2). Importantly, it has previously been shown [15] that the computed effective electronic conductivity depends primarily on the electronic conductivity of the most conducting phase (in this case the binder). Further, it is the relative change in the macroscale conductivity that is of most interest here, and so the exact conductivity is of less importance.

The homogenization calculations for the combined binder-electrolyte phase for the NMC cathode and the HE-NMC cathodes (step (a)(i)→(b) in figure 3), and the homogenization of the combined active particle-electrolyte phase (step (a)(ii)→(b) in figure 3) which is only relevant to the HE-NMC cathode where extremely small electrolyte pores are observed within the active material, were carried out first. These steps are essential precursors to accurately compute the effective conductivity of the whole cathodes owing to the compression algorithm [15], where the narrow electrolyte pathways in the combined binder-active material and combined binder-electrolyte phases would otherwise be lost.

The electronic conductivity of the combined binder-electrolyte phases were found by focusing on a section of each cathode where only binder and electrolyte phases are present, see figure 3 (a)(ii). Two different samples were taken for both types of cathode, having dimensions of around 50×50 pixels and 25 slices corresponding to a cube of dimensions $1.75\mu m \times 1.75\mu m \times 1.75\mu m$. By selecting a sample of this size no compression is needed to form a tractably sized computational grid. In

Table 1: Results of the 'neighbour counting' analysis.

	Probability of finding active material adjacent to binder
HE-NMC (after 1 cycle)	
direction x_1	0.7350
direction x_2	0.7147
direction x_3	0.7844
HE-NMC (after 50 cycles)	
direction x_1	0.6561
direction x_2	0.6133
direction x_3	0.7056
NMC (pristine)	
direction x_1	0.6639
direction x_2	0.7199
direction x_3	0.7133
NMC (after 20 cycles)	
direction x_1	0.5988
direction x_2	0.6505
direction x_3	0.6649

Table 2: Electronic conductivities and volume fractions of each of the material phases.

	Electronic Conductivity $[S \cdot cm^{-1}]$	**NMC Volume Fractions**	**HE-NMC Volume Fractions**
Electrolyte	1×10^{-8}	0.10	0.14
Active material	5×10^{-2}	0.67	0.56
Binder (with carbon black)	5×10^{-1}	0.23	0.30

addition, the effective electronic conductivity of the combined active particle-electrolyte phase was computed for the HE-NMC cathode, see figure 3 (a)(i). To do this, an identically sized sample was taken from the HE-NMC cathode where only active material and electrolyte was present. The results from these calculations are given in table 3.

In order to be able to draw meaningful comparisons between the full homogenization of the pristine and cycled cathodes, it is important to ensure that each pair of samples have nearly identical volume fractions. For instance, if one sample had a larger volume fraction of the high-conducting binder phase, regardless of the geometry, this may produce a larger value of the effective electronic conductivity — thus rendering drawing a comparison between the two samples extremely difficult. The target here is to be able to draw conclusions based strictly on changes in the geometry. Since the FIB process is destructive and different samples must be taken for the pristine and cycled images, finding samples with very similar volume fraction is a non-trivial process and in-house software was developed to identify appropriate sections of each of the sets of FIB images. In the samples studied only one pair of cubes of a suitable size (for both the NMC and HE-NMC cathodes) that had suitably similar volume fractions — to within 0.1% for all three phases — was found. The material phase volume fractions for each pair of cathode samples are reported in table 2 and the conclusions

Table 3: The effective electronic conductivity obtained for the combined binder-electrolyte and combined active particle-electrolyte phases for the NMC and HE-NMC cathodes. In the rightmost column the effective electronic conductivities were normalized by the maximum effective conductivity as calculated using the upper bounds from inequalities (2) and (3) in the Supporting Information.

	Effective Electronic Conductivity $[S \cdot cm^{-1}]$	**Normalized Effective Electronic Conductivity**
NMC B/E Sample 1		
Homogenization (direction x_1)	0.406	0.900
Homogenization (direction x_2)	0.385	0.854
Homogenization (direction x_3)	0.411	0.911
NMC B/E Sample 2		
Homogenization (direction x_1)	0.384	0.848
Homogenization (direction x_2)	0.371	0.819
Homogenization (direction x_3)	0.397	0.876
HE-NMC B/E Sample 1		
Homogenization (direction x_1)	0.346	0.854
Homogenization (direction x_2)	0.343	0.847
Homogenization (direction x_3)	0.365	0.901
HE-NMC B/E Sample 2		
Homogenization (direction x_1)	0.342	0.847
Homogenization (direction x_2)	0.343	0.849
Homogenization (direction x_3)	0.367	0.908
HE-NMC AP/E Sample 1		
Homogenization (direction x_1)	0.043	0.977
Homogenization (direction x_2)	0.043	0.977
Homogenization (direction x_3)	0.043	0.977

below are based solely on a comparison between a pristine (or 1-cycle) versus a more heavily cycled cell for both pair of electrodes. Importantly, the NMC cell and the HE-NMC cathodes have quite different geometries, yet similar trends are observed in both cases.

The effective electronic conductivity was calculated for both pairs of cathodes, by selecting samples (with suitably similar volume fractions) of approximately 500×500 pixels and 250 slices, corresponding to physical dimensions of around $17.5\mu m \times 17.5\mu m \times 17.5\mu m$, and using the combined-phase conductivities shown in table 3. To reduce these samples to a resolution which can be handled computationally on a practical time scale, it was necessary to compress the segmented images by a factor of around 10. However, we emphasize that the amount of geometrical information lost in this process is actually rather small because of the small-scale homogenization steps described above. The results of these final homogenization steps are given in table 4.

Table 4: The effective electronic conductivity obtained for the NMC and HE-NMC cathodes both before and after cycling. In the rightmost column the maximum effective electronic conductivities were normalized by the maximum effective conductivity as calculated using the upper bound from inequality (4) in the Supporting Information and the combined-phase conductivity values listed in table 3.

	Effective Electronic Conductivity $[S \cdot cm^{-1}]$	**Normalized Effective Electronic Conductivity**
HE-NMC (after 1 cycle)		
Homogenization (direction x_1)	0.099	0.727
Homogenization (direction x_2)	0.098	0.720
Homogenization (direction x_3)	0.105	0.771
HE-NMC (after 50 cycles)		
Homogenization (direction x_1)	0.085	0.624
Homogenization (direction x_2)	0.096	0.705
Homogenization (direction x_3)	0.104	0.764
NMC (pristine)		
Homogenization (direction x_1)	0.100	0.761
Homogenization (direction x_2)	0.098	0.745
Homogenization (direction x_3)	0.098	0.745
NMC (after 20 cycles)		
Homogenization (direction x_1)	0.094	0.715
Homogenization (direction x_2)	0.099	0.753
Homogenization (direction x_3)	0.092	0.700

5 Discussion and conclusions

We have presented two different methods for quantifying the impact of geometrical changes that occur in lithium-ion cell cathodes, through cycling, on the electrodes' ability to transmit electronic current. The first method, which was termed 'neighbour counting', has been used to interrogate

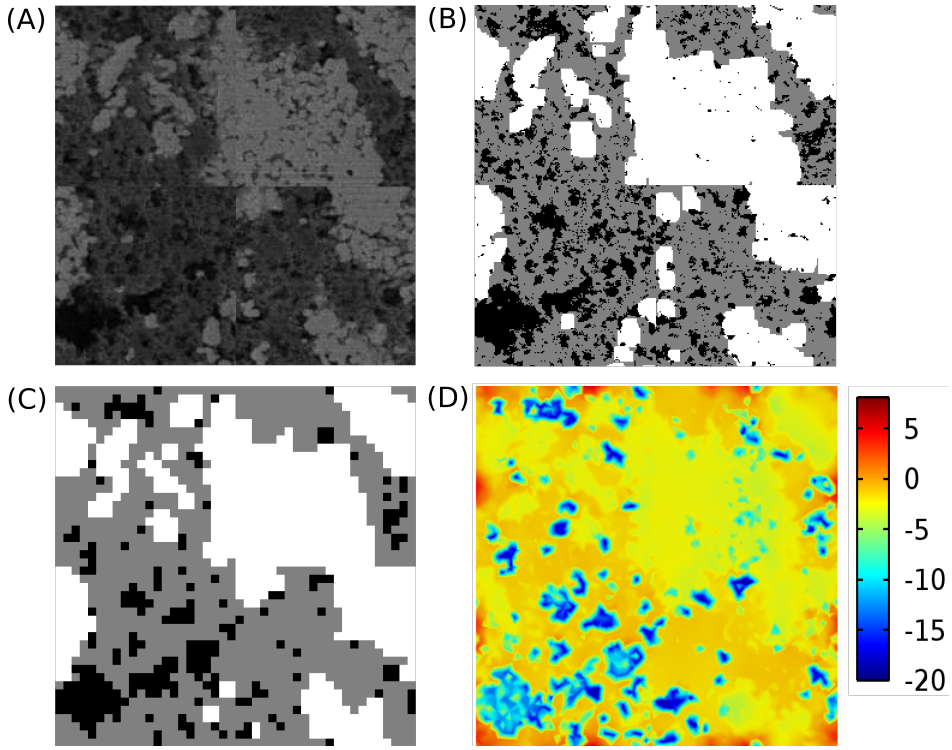

Figure 6: A representative cross section (an x_1-x_2 plane) through the HE-NMC cathode after one cycle. Panel (A) shows the raw FIB image. Panel (B) shows the same image after segmentation. Panel (C) shows the image after compression. Panel (D) shows the logarithm of the modulus of the current density as computed using COMSOL. In this image the current flow is driven by an electric field (of size unity) directed into the page. Note that the sharp discontinuity that appears horizontally and vertically through the centre of these images is an artifact of 'stacking' procedure described in the 'nested homogenization' section.

whether, and to what extent, the binder matrix delaminates from the surfaces of the particles of active material — which could hinder the flow of electrons from the active material into the binder and *vice versa*. The second method, nested homogenization, is an application of a recently developed homogenization-based framework [15] for the determination of effective transport properties of electrochemical systems, in three spatial dimensions, with three material constituents and three distinct length scales. This approach has been used to compute the large-scale effective electronic conductivity of the cathode samples before and after cycling. Thus, this approach gives a macroscale measure of how well the cathodes conduct electrons. For the two sets of lithium-ion battery cathodes studied, the three materials were NMC, PVDF/PTFE-based binder and EC/DMC-based electrolyte, whilst the three length scales were: (i) the length scale of a typical electrolyte pore ($\sim 10 - 50$nm); (ii) the length scale of a typical particle of active material ($\sim 1 - 5\mu$m), and; (iii) the length scale of the entire cathode sample ($\sim 50 - 100\mu$m), (figure 5). In addition to electronic conductivity, the technique presented here can be used to compute a variety of different effective transport coefficients (*e.g.* ionic/thermal diffusivities [15]).

The homogenization-based calculations revealed a drop in effective electronic conductivity, which is a direct result of cycling, in both the NMC and HE-NMC cathodes. Homogenization over the smallest length scale revealed that the presence of the electrolyte pores reduces the conductivity of both the binder and active material phases by around 20% compared to pure binder and active material — compare the values in table 2 with those in table 3. This is both interesting in its own

right and justifies the 'nested' homogenization approach — without it, the effect of the presence of the electrolyte pores would have been lost during the compression needed to form a grid with a resolution that can be handled on a practical time scale. During the next stage of homogenization, the NMC cathode showed a drop in conductivity in two of the three directions (namely x_1 and x_3) of approximately 6%. Similarly, for the HE-NMC cathode, a marked drop in effective electronic conductivity in the x_1 direction of around 14% was observed (figure 7). In addition, the neighbour-counting analysis reveals that these trends are accompanied by a drop of the connectivity between the binder and the active particles resulting from the delamination of the binder. The NMC cell has been cycled 20 times (at rates of C/30 and C/10 each for 10 cycles), in contrast, the HE-NMC cathode has been cycled 50 times (at the larger rate of C/3), hence the lesser decrease in effective electronic conductivity in the NMC cathode might be attributed to the less abusive cycling conditions. Given that this relatively small, yet non-negligible, effect is observed over a modest number of cycles, it is not unreasonable to expect that over a larger number of cycles the loss of electrical conductivity (due to the delamination of the binder) could become so large as to limit the performance of the battery by hindering the transport of electrons between the active material and the current collector via the binder matrix.

We also note that the way in which the half cell architecture was constructed is such that the current flows predominantly in the x_1 direction – the direction perpendicular to both current collectors. Given the large disparity in length scales in the half cell — the cell dimensions are much larger in the x_2 and x_3 directions ($\sim$ 1cm) than in the x_1 direction ($\sim 100\mu$m) — is it reasonable to expect that the swelling, and subsequent contraction, of the active material that occurs as a result of (de-)lithiation has the largest effect in the x_1 direction. We therefore conjecture that the underlying reason for the large drop in electronic conductivity in the x_1 direction are the larger volumetric changes that occur in that direction causing the binder to deform and detach from the surface of the active material. A separate investigation is currently underway, in which a coupled solid-fluid mechanics model is being developed, that aims to understand the mechanical conditions that the composite cathode experiences during cycling. A key question we seek to address concerns how the material properties of the binder phase and the conditions characterizing the cell assembly affect the detrimental process described in this study. Preliminary insights from this analysis appear very interesting and will be reported in the near future.

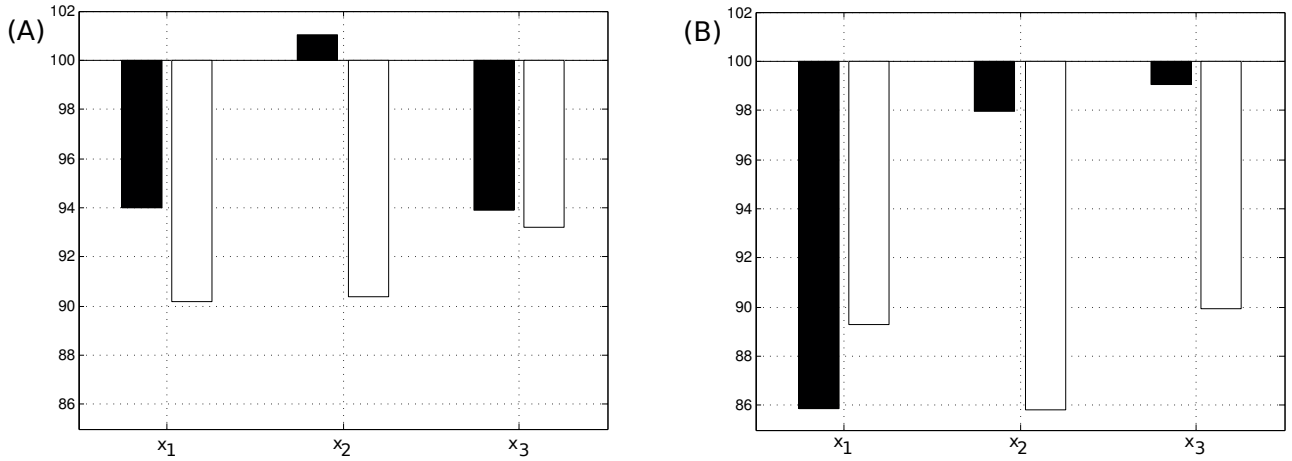

Figure 7: A summary of the relative (percentage) change in effective conductivity and connectivity as a result of cycling. Panels (A) and (B) show the results for the NMC and HE-NMC cathodes respectively, and the black and white bars are the results as calculated by the nested homogenization method (effective conductivity) and neighbour-counting methods (connectivity), respectively.

Acknowledgements

JF, AG, HL, SK, SS, GC, BG and BP would like to thank the Automotive Partnership Canada (APC) and General Motors of Canada (GMC) who funded this research. The electron microscopy data included in this paper was acquired at the Canadian Centre for Electron Microscopy, a national facility supported by the Natural Sciences and Engineering Research Council of Canada (NSERC) and McMaster University. The authors thank Giles Richardson (University of Southampton) who motivated the 'neighbour-counting' argument and is currently helping to develop the mechanistic model which aims to explain the findings of this work.

References

[1] P. Arora & R. E. White. Capacity fade mechanisms and side reactions in lithium-ion batteries. *J. Electrochem. Soc.*, 10:3647–3667, 1998.

[2] A. Bensoussan, J. L. Lions and G. Papanicolau. Asymptotic analysis for periodic structures. North-Holland, Amsterdam, 1978.

[3] D. J. Bergman. The dielectric constant of a composite material – A problem in classical physics. *Phys. Rep. C*, 43(9):377–407, 1978.

[4] A. Cherkaev. *Variational Methods for Structural Optimization*, volume 140 of *Applied Mathematical Sciences*. Springer-Verlag, New York, 2000.

[5] COMSOL Multiphysics simulation software. information available at http://www.comsol.com.

[6] M. Doyle and J. Newman. Analysis of capacity-rate for lithium batteries using simplified models of the discharge process. *J. Appl. Electrochem.*, 27:846–856, 1996.

[7] M. Doyle and J. Newman. Comparison of modeling predictions with experimental data from plastic lithium ion cells. *J. Electrochem. Soc.*, 143:1890–1903, 1996.

[8] T. F. Fuller, M. Doyle, J. Newman. Relaxation phenomena in lithium-ion insertion cells. *J. Electrochem. Soc.* 143:982–990, 1994.

[9] T. F. Fuller, M. Doyle and J. Newman. Simulation and optimisation of the dual lithium insertion cell. *J. Electrochem. Soc.*, 141:1–10, 1994.

[10] K. Golden. Bounds on the complex permittivity of a multicomponent material. *Journal of the Mechanics and Physics of Solids*, 34(4):333–358, 1986.

[11] K. Golden. Bounds on the complex permittivity of sea ice. *J. Geophys. Res. (Oceans)*, 100(C7):13,699 – 13,711, 1995.

[12] K. Golden and G. Papanicolaou. Bounds for effective parameters of heterogeneous media by analytic continuation. *Comm. Math. Phys.*, 90:473–491, 1983.

[13] K. M. Golden. The interaction of microwaves with sea ice. In G. Papanicolaou, editor, *Wave Propagation in Complex Media, IMA Volumes in Mathematics and its Applications, Vol. 96*, pages 75 – 94. Springer-Verlag, 1997.

[14] A. Gully, L.G.E. Backstrom, H. Eicken, and K.M. Golden. Complex bounds and microstructural recovery from measurements of sea ice permittivity. *Physica B*, 394:357–362, 2007.

[15] A. Gully, H. Liu, S. Srinivasan, A. K. Sethurajan, S. Schougaard & B. Protas. Effective transport properties of porous electrochemical materials - a homogenization approach. *J. Electrochem. Soc.*, 161(8):3066-3077, 2014.

[16] W. Lai and F. Ciucci. Mathematical modeling of porous battery electrodes - revisit of Newman's model. *Electrochim. Acta.* 56:4369–4377, 2011.

[17] D. Lukkassen, G. Nguetseng, H. Nnang and P. Wall. Reiterated homogenization of nonlinear monotone operators in a general deterministic setting. *J. Func. Spac. Appl.*, 2:121–152, 2009.

[18] N. Meunier and J. V. Schaftingen. Periodic reiterated homogenization for elliptic functions. *J. Math. Pures. Appl.*, 84:1716–1743, 2005.

[19] G. W. Milton. Theoretical studies of the transport properties of inhomogeneous media. Technical Report Physics IV, Dept. of Theor. Phys., Univ. of Sydney, 1979.

[20] G. W. Milton. Bounds on the complex permittivity of a two-component composite material. *J. Appl. Phys.*, 52:5286–5293, 1981.

[21] G. W. Milton. Concerning bounds on the transport and mechanical properties of multicomponent composite materials. *Applied Physics A*, 26(2):125–130, 1981.

[22] G. W. Milton. *Theory of Composites.* Cambridge University Press, Cambridge, 2002.

[23] G. J. Nelson, W. M. Harris, J. L. Lombardo, and et al. Comparison of SOFC cathode microstructure quantified using X-ray nanotomography and focused ion beam-scanning electron microscopy. *Electrochem. Commun.*, 13:586–589, 2011.

[24] J. S. Newman. Electrochemical systems, 3rd edn. Prentice Hall, New Jersey, 2004.

[25] G. Richardson, G. Denuault, and C. P. Please. Multiscale modelling and analysis of lithium-ion battery charge and discharge. *Journal of Engineering Mathematics*, 72:41–72, 2012.

[26] M. Schmuck and P. Berg. Effective macroscopic equations for species transport and reactions in porous catalyst layers. *J. Electrochem. Soc.* 161(8):E3323–E3327, 2014.

[27] S. Torquato. *Random Heterogeneous Materials: Microstructure and Macroscopic Properties.* Springer-Verlag, New York, 2002.